ROYAL SOCIETY OF CHEMISTRY

PAPER

Check for updates

Ionic liquid-modified perovskite films for enhanced solar cell stability

Udit Tiwari, [iD] *[ab] Jordan Cole, [iD] †[a] Zheshen Li, [iD] [c] Alex Walton, [iD] [de] Liam P. Dwyer, [iD] [fg] Ben F. Spencer, [iD] [fg] Sergey Zlatogorsky [iD] [h] and Karen L. Syres [iD] *[a]

Halide perovskites have emerged as promising candidates for photovoltaic applications due to their remarkable device efficiencies. Despite this progress, their commercial viability is hindered by structural instability under high temperature and humidity. Here, the stability of mixed-halide perovskites is enhanced by incorporating the ionic liquids (ILs) 1-butyl-3-methylimidazolium tetrafluoroborate (BMIMBF$_4$) and 1-butyl-3-methylimidazolium chloride (BMIMCl). The resistance of the IL-modified films to heat and moisture is investigated using X-ray photoelectron spectroscopy (XPS), near edge X-ray absorption fine structure (NEXAFS), hard X-ray photoelectron spectroscopy (HAXPES) and near-ambient pressure X-ray photoelectron spectroscopy (NAP-XPS). Additionally, the role of a SnO$_2$ electron transport layer (ETL) is investigated for improving the stability of the IL-modified films. Results indicate that the IL-modified perovskite films on SnO$_2$ demonstrate enhanced thermal stability, withstanding temperatures of at least 300 °C. BMIMBF$_4$-modified films demonstrate superior thermal stability, attributed to the formation of an IL overlayer which protects the underlying perovskite layer. Conversely, in BMIMCl-modified films, BMIM$^+$ and Cl$^-$ ions diffuse into perovskite grain boundaries, enhancing crystallinity and neutralising surface defects. HAXPES results show that IL-modification protects the perovskite films from surface degradation. NAP-XPS results indicate that BMIMCl-modified films show greater resistance to water penetration than BMIMBF$_4$-modified films. It is inferred that the combined use of ILs and SnO$_2$ significantly enhances the thermal and moisture stability of perovskites, advancing their potential for commercial application.

1. Introduction

Halide perovskite solar cells (PSCs) have emerged as frontrunners in next-generation photovoltaic technology due to their high efficiency and ease of fabrication.[1] Despite these advantages, their practical deployment is hindered by their susceptibility to environmental stressors such as high temperature and moisture.[2–5] Addressing the instability of

perovskite thin films is crucial for ensuring their long-term performance and commercial viability. Several strategies have been explored to enhance perovskite stability, including additive engineering, hydrophobic interlayers, and halide substitution.[4,6,7] Among these, additive engineering has shown particular promise in stabilising perovskite structures and mitigating defects. In this study, we examine the impact of incorporating ILs, BMIMCl (1-butyl-3-methylimidazolium chloride) and BMIMBF$_4$ (1-butyl-3-methylimidazolium tetrafluoroborate) into mixed-halide perovskite CH$_3$NH$_3$PbI$_{3-x}$Cl$_x$ (MAPbI$_{3-x}$Cl$_x$, methylammonium lead iodide–chloride) thin films. Our objectives are twofold: first, to enhance film quality by modifying the crystallisation process, and second, to improve resistance to environmental stressors by using ILs that may form protective layers through strong coordinate bonds. We assess the effects of BMIMBF$_4$ and BMIMCl on the crystallisation and stability of MAPbI$_{3-x}$Cl$_x$ films, both with and without a SnO$_2$ electron transport layer (ETL). ILs have also been used as interfacial modifiers in devices (rather than additives in the perovskite precursor solution) and this has been shown to improve energy level matching and passivate defects at interfaces.[8,9] MAPbI$_{3-x}$Cl$_x$ perovskite solar cells offer distinct advantages over pure MAPbI$_3$ counterparts, including

[a] Jeremiah Horrocks Institute for Mathematics, Physics and Astronomy, University of Lancashire, Preston, PR1 2HE, UK. E-mail: utiwari2@uclan.ac.uk, KSyres@lancashire.ac.uk

[b] School of Medicine and Dentistry, University of Lancashire, Preston, PR1 2HE, UK

[c] Department of Physics and Astronomy, University of Aarhus, Ny Munkegade, DK-8000 Aarhus C, Denmark

[d] Department of Chemistry, School of Natural Science, The University of Manchester, Oxford Road, Manchester, M13 9PL, UK

[e] Photon Science Institute, University of Manchester, Manchester M13 9PL, UK

[f] Department of Materials, School of Natural Sciences, The University of Manchester, Manchester, M13 9PL, UK

[g] Henry Royce Institute, University of Manchester, Manchester M13 9PL, UK

[h] Institute of Materials and Investigative Sciences, University of Lancashire, Preston, PR1 2HE, UK

† Present addresses: Nanoco Technologies Ltd, Science Centre, The Heath Business & Technical Park, Runcorn, WA7 4QX, UK.

a significantly longer charge carrier diffusion length – approximately ten times greater – which enhances charge collection efficiency and reproducibility.[10] Unlike MAPbI₃, which typically requires mesostructured cells for optimal performance, MAPbI$_{3-x}$Cl$_x$ can achieve high power conversion efficiencies (PCEs) in planar device structures through simpler fabrication methods.[11]

ILs are advantageous due to their broad liquid temperature range, high carrier mobility, and thermal and electrochemical stability.[12] Their structural versatility allows diverse interactions with perovskite materials, potentially enhancing film quality and stability. Previous studies have demonstrated that incorporating ILs into PSCs can improve device performance by creating halide complexes or optimising energy level alignment at interfaces.[13,14] Snaith *et al.* reported that BMIM$^+$ cations effectively bind to surface sites vulnerable to heat and moisture, thus improving PSC stability.[15] Their work showed that devices with 0.3 mol% BMIMBF₄ achieved a high PCE of 19.8%. Building on this, our study explores 0.3 mol% IL-modified perovskite films on exposure to high temperatures and moisture. When exposed to stressors such as heat, UV light and moisture, pure MAPbI₃ (CH₃NH₃PbI₃) can decompose into MAI (CH₃NH₃I) + PbI₂. MAI can further decompose into CH₃NH₂ + HI, and PbI₂ can further decompose into Pb + I₂.[16] MAPbI$_{3-x}$Cl$_x$ used in this study can also form the corresponding Cl species *e.g.* CH₃NH₃Cl (MACl) + PbCl₂, and possibly mixed halide species such as PbICl.[17]

It has been reported that BMIMBF₄ enhances device performance by integrating BF$_4^-$ ions into the perovskite lattice. Previous studies indicate that BF$_4^-$ ions reduce trap density, lower recombination rates and extend photoluminescence lifetime.[18,19] The role of chlorine ions in MAPbI$_{3-x}$Cl$_x$ perovskites remains debated. Some studies suggest that Cl$^-$ ions do not integrate into the PbI₃ lattice but instead enhance performance through indirect mechanisms, such as improved charge transport or enhanced crystallinity.[11,17,20,21] Other studies support the incorporation of Cl$^-$ ions into the lattice, affecting material properties.[22,23] Our investigation focuses on how BMIMCl, a chloride-containing IL, influences MAPbI$_{3-x}$Cl$_x$ crystallisation and the effects of excess Cl$^-$ ions on the incorporation of Cl into the perovskite lattice. By comparing BMIMCl and BMIMBF₄, we aim to isolate the specific contributions of the chloride anion to perovskite film quality and stability.

Our study highlights the role of imidazolium-based ILs, BMIMBF₄ and BMIMCl, in enhancing the stability of mixed halide perovskite MAPbI$_{3-x}$Cl$_x$ films against moisture and heat. We find that the IL-modified perovskite films deposited on SnO₂-coated substrates demonstrate resistance to thermal degradation, maintaining their structural integrity even at elevated temperatures of up to 300 °C. We attribute this enhanced thermal stability to the interaction between the IL and the SnO₂. 300 °C was chosen as the testing temperature to induce degradation and assess the stabilising effect of the IL modification. Hard X-ray photoelectron spectroscopy

(HAXPES) results show that IL-modification protects the perovskite films from surface degradation. The moisture endurance of these IL-modified films, assessed *via* near-ambient pressure X-ray photoelectron spectroscopy (NAP-XPS), reveals superior resistance to water exposure, particularly for the BMIMCl-modified perovskite. This improved stability aligns with the hypothesised interaction mechanisms between the ILs, perovskite and SnO₂, further underscoring the potential of ILs in prolonging the operational lifespan of perovskite-based devices. The findings presented here contribute to understanding how ILs and SnO₂ may help mitigate degradation pathways in perovskite films, offering insights that could aid in the development of more durable perovskite solar cells.

2. Experimental

2.1 Materials and deposition

MAPbI$_{3-x}$Cl$_x$ perovskite precursor ink (I101) in dimethylformamide (DMF) was purchased from Ossila Ltd. (Sheffield, UK), and all other chemicals were sourced from Sigma-Aldrich (Gillingham, UK), Thermo Scientific (Abingdon, UK) or Ossila Ltd. Films were fabricated on titanium foil substrates, which were cleaned sequentially (details in SI). The substrates were divided into two sets: one set was spin-coated with a 15% SnO₂ solution in H₂O (50 µl, 3000 rpm, 30 s) and annealed at 150 °C for 40 minutes, the other set was not coated with SnO₂. The perovskite precursor ink was heated at 70 °C for 2 hours to ensure complete solute dissolution. Two perovskite solutions were prepared, one containing 0.3 mol% BMIMCl and the other containing 0.3 mol% BMIMBF₄ and heated at 70 °C for 10 minutes. These two solutions, along with the pure perovskite ink, were spin-coated onto six titanium substrates (three with SnO₂ and three without) at 3000 rpm for 30 seconds (see Fig. S1 in SI). The substrates were then annealed at 90 °C for 120 minutes and stored in a nitrogen-filled glovebox. A fresh batch of samples was prepared specifically for the ASTRID, HAXPES, and NAP-XPS experiments.

2.2 XPS measurements

XPS measurements were conducted at the AU-Matline end station at ASTRID-2, ISA, Denmark, using a Scienta electron energy analyser. The ultra-high vacuum (UHV) chamber had a base pressure below 1×10^{-9} Torr. XPS scans were taken before and after heating samples to 100 °C, 150 °C, and 300 °C. Initial studies showed minimal X-ray beam damage during the time needed to record a set of XPS scans, therefore, the sample position was moved by 100 µm at each temperature setting to minimise any potential beam damage. Photon energies used for the XPS spectra are listed in Table S1. Core level scans were recorded at normal emission with a pass energy of 20 eV. The combined beamline and analyser resolution values for the core levels are 0.39 eV for C 1s at 380 eV, 0.32 eV for Pb 4f at 320 eV, 0.19 eV for I 4d at 120 eV and 0.32 eV for Cl 2p at 320 eV. Spectra were charge-

© 2025 The Author(s). Published by the Royal Society of Chemistry

RSC Appl. Interfaces, 2025, **2**, 1674–1689 | 1675

corrected to adventitious carbon at 285.0 eV. Data were processed using Shirley background subtraction and Gaussian–Lorentzian line shapes (GL30) in CasaXPS, with binding energy (BE) values accurate to ±0.1 eV.

2.3 Work function measurements

For work function measurements at AU-Matline, the secondary electron cut-off (SECO) spectra for the films were recorded using a 50 eV photon energy X-ray beam with analyser pass energy of 20 eV. A negative bias was applied to the samples using a 9 V battery. The applied bias was measured to 2 decimal places for each work function measurement. At the beginning of the AU-Matline experiments, a Fermi edge was recorded from gold foil in contact with the sample plate. This Fermi edge was fit using SpecsLab Prodigy software and the work function value in the Scienta analyser software was calibrated to this position. Therefore, the BE of the Fermi edge was set to zero and the work function becomes $\hbar\omega - BE_{SECO}$,[24] where $\hbar\omega$ is the photon energy and BE_{SECO} is the binding energy of the SECO. In practice, the applied bias was subtracted from the measured kinetic energy values, and the SECO spectra plotted for all samples, as shown in Fig. S2 (a–f). Work function values were extracted from the SECO spectra, determined by the linear extrapolation of the secondary edge slope to the kinetic energy axis.

2.4 NEXAFS measurements

NEXAFS measurements were performed on the AU-Matline beamline at ASTRID-2, Aarhus, Denmark. Carbon K-edge (280–320 eV) and nitrogen K-edge (395–420 eV) spectra were recorded at 45° incidence with a base pressure of ~4 × 10⁻¹⁰ mbar. Spectra were acquired in constant final state mode at 100 eV pass energy, detecting Auger electrons at kinetic energies of 270 eV (C K-edge) and 380 eV (N K-edge). Photon energies at the beamline were calibrated with second order incoming light with maximum errors of ±0.1 eV for the whole range and a typical error of 0.05 eV. The energy resolution of the photon source varies with photon energy. Over the C K edge the energy resolution is approximately 0.23 eV and over the N K edge the energy resolution is approximately 0.36 eV. Data analysis was carried out using Igor Pro software.

2.5 AR-HAXPES measurements

AR-HAXPES was used to study the elemental composition and depth profiles of the films at the Henry Royce Institute, Manchester, UK. The high-throughput HAXPES-Lab instrument (Scienta Omicron GmbH) utilised a micro-focussed Ga Kα metal jet X-ray source (9.25 keV) and an EW-4000 electron energy analyser. Measurements were taken in transmission mode at normal emission (0° w.r.t analyser normal) and in angular mode at grazing emission (40° w.r.t analyser normal). Core level spectra were recorded with a pass energy of 200 eV and an analyser slit width of 0.8 mm. The energy resolution of the spectrometer was previously

determined by measuring the 16/84% width of the Fermi edge from a gold foil.[25] The resolution is approximately 0.8 eV for these pass energy and slit settings. At grazing emission, a series of spectra were obtained over a range of photoelectron emission angles (15–65° w.r.t the surface normal), probing different sampling depths (see section 5 and 6 in SI).[26] Quantification was performed using theoretical sensitivity factors.[27]

2.6 NAP-XPS measurements

NAP-XPS measurements were conducted using a SPECS Focus 500 monochromated Al Kα source (1486.6 eV) and a SPECS Phoibos 150 NAP analyser. Measurements were performed under ultrahigh vacuum (UHV) and near-ambient pressure (NAP) conditions, with the NAP cell filled with H_2O vapour to stabilise pressure at ~4.5 mbar (RH ~15%). Samples were exposed to water vapor for ~10 hours, with 25 scans taken for each core level at 25 °C. XPS spectra were recorded before, during, and after exposure to water. The sample position was moved by 300 μm between sets of scans to minimise beam damage. BE values were charge-corrected with reference to the Sn $3d_{5/2}$ peak at 488.0 eV. All spectra were processed with Shirley background subtraction and fitted using CasaXPS with GL(30) line shapes, with binding energy (BE) values accurate to ±0.1 eV.[28] Survey spectra are taken at a pass energy of 60 eV while the core level spectra were recorded at 30 eV pass energy. In the NAP cell, the FWHM of a Ag $3d_{5/2}$ peak at pass energy 30 eV is approximately 0.8 eV. Quantification was performed using built-in CasaXPS sensitivity factors.

3. Results and discussion

XPS results

The C 1s XPS spectra for the two sets of samples (with and without a SnO_2 layer) are shown in Fig. 2. In all the spectra, peaks fitted at 285.0 eV are attributed to hydrocarbon contamination[29] or the IL aliphatic C–C bonds (labelled C4 in Fig. 1). The peaks fitted at 286.0 eV correspond to an aliphatic C–N bond. In the perovskite films, this could arise from the unreacted/dissociated precursor CH_3NH_3I (MAI).[30–32] In the perovskite films modified with ILs, the 286.0 eV peak could also originate from the aliphatic C–N bond (C3 in Fig. 1) within the BMIM group.[30]

The peaks at 286.6 eV can be attributed to both the perovskite C–N bond (in the perovskite lattice) and the aromatic C–C–N carbons (labelled C2 in Fig. 1) in the ILs.[33,34] The imidazolic N–C–N carbon (labelled C1 in Fig. 1) exhibits a peak at 287.3 eV.[30] However, in pure perovskite films, the peaks at 287.3 eV at 300 °C are likely associated with the formation of methylamine (CH_3NH_2) due to the thermal decomposition of MAI (CH_3NH_3I) and/or perovskite. The peaks at 287.7 eV can be assigned to C=O groups formed due to surface oxidation of the film.[35] Similarly, high energy peaks in the range of 288.5 eV to 289.5 eV can be assigned to the O–C=O group, indicating oxidative decomposition.[36–39]

Binding Energy	Peak Assignment
285.0 eV	Adventitious carbon or C4
286.0 eV	C-N in CH_3NH_3 or C3 in BMIM group
286.6 eV	C-N in Perovskite or C2 in BMIM group
287.3 eV	C-N in CH_3NH_2 or C1 in BMIM group
287.7 eV	C=O
288.5–289.5 eV	O-C=O

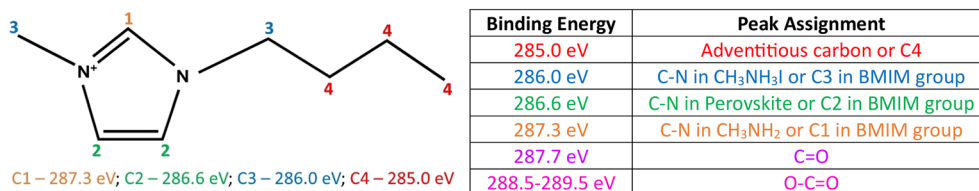C1 – 287.3 eV; C2 – 286.6 eV; C3 – 286.0 eV; C4 – 285.0 eV

Fig. 1 Chemical structure of the BMIM cation showing 4 distinct carbon environments labelled 1–4 (left) and the C 1s peak assignments (right).

All the peak assignments in the C 1s spectra are tabulated in Fig. 1.

The XPS spectra for pure perovskite films, with and without the SnO_2 layer (Fig. 2(a) and (b)), show peaks for MAI, perovskite, C=O, and O–C=O up to 150 °C. As temperature increases, the MAI peak intensifies, indicating perovskite degradation. At 300 °C, C=O and O–C=O peaks disappear, and a CH_3NH_2 peak at 287.3 eV emerges, confirming the decomposition of perovskite into methylamine. The SnO_2/$BMIMBF_4$-perovskite film (Fig. 2(f)) retains the perovskite peak (286.6 eV) even at 300 °C, while in the $BMIMBF_4$-perovskite film (Fig. 2(e)), this peak is stable only up to 150 °C, giving way to new low BE peaks at 282.3 eV and 283.7 eV at 300 °C. The SnO_2/$BMIMBF_4$-perovskite film also shows a low BE peak at 283.7 eV at 300 °C. These emerging features could indicate the formation of boron–carbide bonds, indicating significant chemical changes in the films at higher temperatures.[40] Similarly, in the BMIMCl-perovskite film (Fig. 2(c)), the

perovskite peak persists only up to 150 °C while the SnO_2/BMIMCl-perovskite film (Fig. 2(d)) retains the perovskite peak even at 300 °C. This suggests that both SnO_2 and IL in combination play a part in preserving the perovskite under higher temperature, but IL/SnO_2 alone does not.

Fig. 3 illustrates the I 4d spectra of the six films. Each graph shows spectra taken before heating and at the three temperature settings. The two peaks arise from the spin–orbit splitting (splitting energy = ~2.0 eV) of the d orbital and are assigned to I $4d_{3/2}$ and I $4d_{5/2}$. Components were fitted to the data by constraining the areas of the I $4d_{3/2}$ and I $4d_{5/2}$ to the correct ratio (2 : 3). For some films, this resulted in a poor fit to the experimental data for the higher BE peak (I $4d_{3/2}$). Doublets are often difficult to fit using Voigt curves and since we focus here on shifts in BE, the fit is sufficient to follow the trends in the data. BEs of the I $4d_{5/2}$ component for all films, plotted in Fig. 3, are provided in Table S2 of the SI. The perovskite I $4d_{5/2}$ peak position has been reported in previous studies at ~49.5
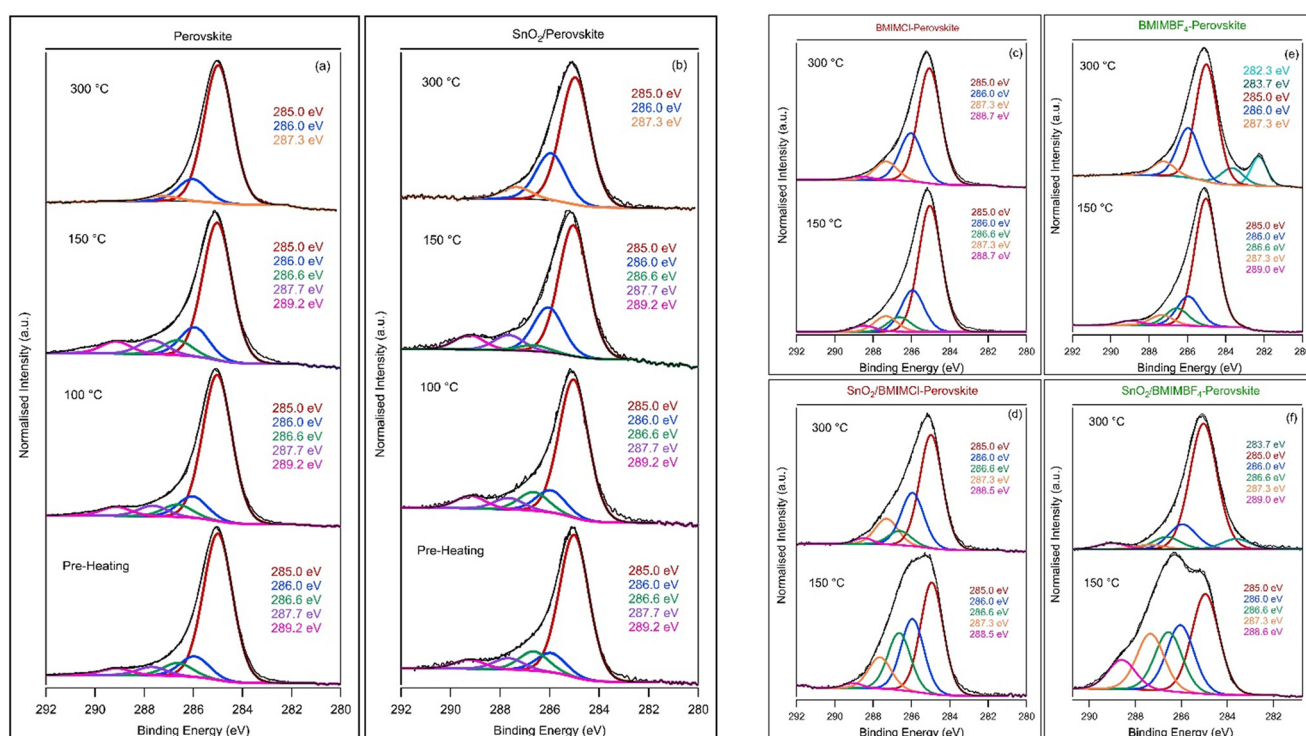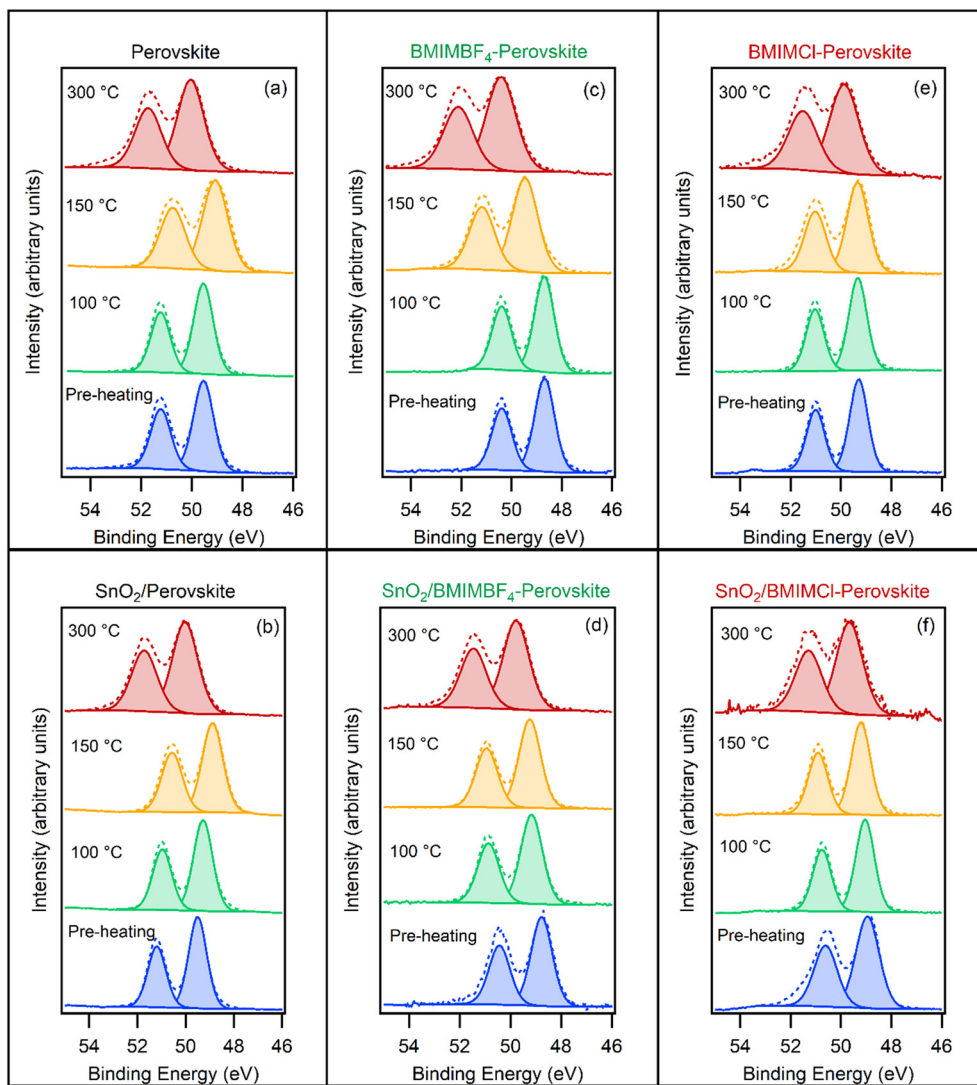

Fig. 2 High-resolution C 1s core level XPS spectra of the pure ((a) and (b)) and IL-modified ((c)–(f)) perovskite films deposited on Ti foil ((a), (c) and (e)) and SnO_2 coated Ti foil ((b), (d) and (f)). Peak intensities are normalised to the intensity of the adventitious carbon peak. BEs of fitted peaks are shown next to each spectrum and a summary of C 1s peak assignments is shown in Fig. 1.
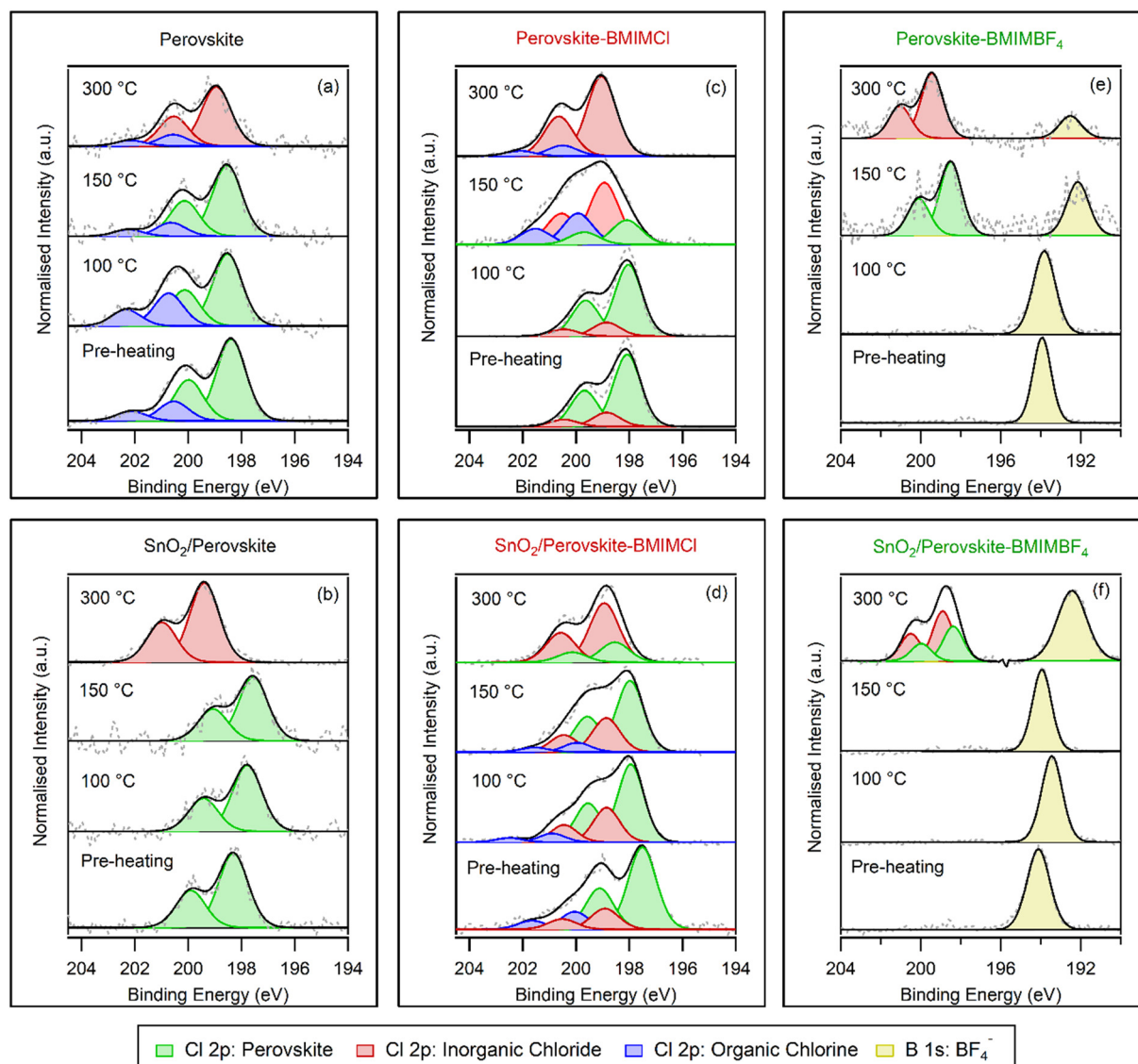
Fig. 3 High-resolution I 4d core level XPS spectra of pure ((a) and (b)) and IL-modified ((c)–(f)) perovskite films deposited on Ti foil ((a), (c) and (e)) and SnO$_2$ coated Ti foil ((b), (d) and (f)). The dotted lines represent the raw data and the coloured areas represent the fitted components. Spectra have been normalised to the intensity of the I 4d$_{5/2}$ peak.

eV.[29,41] The BE values exhibit relatively stable behaviour as the samples are heated to 100 °C, but undergo a non-uniform shift in BE as the temperature is raised to 150 °C, with BEs ranging from 48.7 eV to 49.5 eV. In contrast, a clear upward shift in BE values is observed when the temperature is raised to 300 °C indicating a change in the chemical environment of iodine, possibly indicating dissociation from the $(PbI_6)^{-4}$ octahedra of the perovskite lattice. Of particular interest is the observation that the SnO$_2$/IL-modified perovskite films (d & f) exhibit the smallest increase in BE after heating to 300 °C. The I 4d spectra for all samples at 300 °C show a noticeable increase in the FWHM. It has previously been observed that I 3d spectra of degraded perovskite samples show an increased FWHM and this was attributed to the loss of iodine from the perovskite crystal structure in the form of I$_2$ or HI.[42] We speculate that the broadening of the I 4d peaks in our data

could indicate that I$^-$ ions are migrating away from their position in the perovskite lattice. Ion migration in perovskites has been extensively studied and can be driven by light, temperature and instability of the perovskite.[43,44] The broadening is least pronounced in the IL-modified films with SnO$_2$, suggesting that the IL-SnO$_2$ interaction helps to stabilise the perovskite structure and further supports the enhanced thermal stability of the films.

The Cl 2p XPS spectra of the films, shown in Fig. 4, reveal a characteristic doublet structure for Cl 2p$_{3/2}$ and Cl 2p$_{1/2}$ components. Cl 2p$_{3/2}$ peaks between 197.5 and 198.5 eV correspond to the perovskite structure,[17,29,45] while those between 198.9 and 199.4 eV are attributed to inorganic chloride,[46] potentially from unreacted or decomposed PbCl$_2$. Peaks at 199.9 to 200.9 eV indicate organic chlorine, possibly from CH$_3$NH$_3$Cl formed during thermal degradation. In the perovskite film (Fig. 4a), Cl 2p doublet peaks from perovskite

© 2025 The Author(s). Published by the Royal Society of Chemistry

Fig. 4 High-resolution Cl 2p core level XPS spectra of pure ((a) and (b)) and IL-modified ((c)–(f)) perovskite films deposited on Ti foil (a), (c) and (e)) and SnO$_2$ coated Ti foil ((b), (d) and (f)). Cl 2p$_{3/2}$ peaks between 197.5 and 198.5 eV correspond to the perovskite structure, peaks between 198.9 and 199.4 eV are attributed to inorganic chloride and peaks between 199.9 to 200.9 eV indicate organic chlorine. For BMIMBF$_4$-modified perovskite films, the B 1s level is shown in the same spectrum and arises from the BF$_4$ anion.

and organic chlorine are observed pre-heating. The perovskite peaks are visible up to 150 °C but shift to higher BE at 300 °C, suggesting chlorine detachment and potential PbCl$_2$ formation. The SnO$_2$/perovskite film (Fig. 4b) lacks organic chlorine peaks and exhibits a similar shift from perovskite to inorganic chloride peaks after 150 °C. For the BMIMCl-modified perovskite films we also expect a Cl signal due to the presence of Cl from the IL. The Cl 2p signal from pure BMIMCl has been reported in the literature at 197.2 eV (ref. 47) but we do not observe any features at this BE. This suggests that the Cl$^-$ ions have either been incorporated into the perovskite or may have formed organic/inorganic species (and now contribute to those peaks). The SnO$_2$/BMIMCl-perovskite film (Fig. 4d) shows significant organic and inorganic Cl species prior to heating but retains a stable

perovskite doublet up to 150 °C, with a lower-intensity perovskite doublet still present at 300 °C. In contrast, the BMIMCl-perovskite film (Fig. 4c) maintains perovskite peaks only until 150 °C; at 300 °C these peaks disappear and inorganic chloride peaks dominate, indicating significant decomposition into lead halides.

For the BMIMBF$_4$-modified perovskite films, the BE window was widened during XPS measurements to display both Cl 2p and B 1s in the same spectrum. In the BMIMBF$_4$-perovskite film (Fig. 4e), a distinct B 1s peak at 193.9 eV is observed both before and after heating to 100 °C, with no Cl 2p peaks present. This B 1s peak indicates the presence of the BF$_4^-$ ion from the IL. The absence of a Cl 2p signal and the observation of a strong B 1s signal could indicate that the perovskite Cl atoms are buried beneath the IL BF$_4^-$ ions. At

150 °C, perovskite Cl 2p doublet peaks appear at 198.5 eV and 200.1 eV, while the B 1 s peak shifts to 192.1 eV, indicating a change in chemical environment. The appearance of the Cl 2p peaks suggests there is some rearrangement in the layer and the Cl atoms are no longer buried beneath the BF_4^- ions. The shift of the B 1s peak to lower BE could indicate interaction of the BF_4^- anion with perovskite at high temperature to form boron–carbide bonds. Low BE peaks were also observed in the C 1s spectra for the BMIMBF$_4$-modified perovskite films at high temperature which supports this assignment. At 300 °C, the Cl 2p peaks shift by +0.4 eV, suggesting decomposition of the perovskite into lead halides. In the SnO$_2$/BMIMBF$_4$-perovskite film (Fig. 4f), a sharp B 1s peak is observed up to 150 °C, with no Cl 2p peaks visible. At 300 °C, the B 1s peak broadens and shifts to 192.4 eV, while Cl 2p peaks emerge, revealing a higher-intensity inorganic chloride doublet (198.9 eV and 200.5 eV) and a lower-intensity perovskite doublet (198.5 eV and 200.1 eV). Again, this indicates the interaction of the BF_4^- anion with perovskite at high temperature. We propose that at room temperature, BMIMBF$_4$ forms a protective overlayer that attenuates the Cl signal coming from the perovskite beneath it. Imidazolium based ILs have been shown to form a layer of cations at the IL-vacuum interface with alkyl chains of the cations facing outwards towards the vacuum.[30] The sudden appearance of the Cl 2p peaks at high temperature indicates the disintegration of the protective overlayer, leading to the exposure of the underlying perovskite layer.

Work function measurements

The work function of the perovskite and IL-modified perovskite films was assessed using SECO measurements, the

results of which are plotted as a function of temperature in Fig. 5. The work function values were extracted from the SECO spectra (refer to Fig. S2 in SI) with an uncertainty of ±0.05 eV. The work function values of the perovskite closely align with the literature-reported value of ~3.90 eV.[48] The SnO$_2$/perovskite film exhibits a work function of 4.1 eV before heating. This value remains constant at 4.1 eV up to 150 °C, then slightly decreases to 4.0 eV after heating the sample to 300 °C. Similarly, the perovskite film also maintains a constant value of 4.0 eV until 150 °C, after which it decreases to 3.7 eV when heated to 300 °C. This decrease in the work function values after heating the samples to 300 °C may be attributed to the thermal decomposition of the perovskite as observed in the XPS analysis. The nearly constant work function values in the SnO$_2$ coated sample could suggest that SnO$_2$ serves as a thermally stable ETL.

Prior to heating, the BMIMCl-perovskite film has the same work function as the pure perovskite film at 4.0 eV. Upon increasing the temperature to 100 °C, the work function reduces to 3.4 eV. This suggests that heating is important for the interaction of BMIMCl with the perovskite. The work function decreases further to 3.1 eV as the temperature is increased to 150 °C. However, upon increasing the temperature to 300 °C, the work function increases slightly to 3.4 eV. The SnO$_2$/BMIMCl-perovskite film demonstrates a lower work function of 3.8 eV up to 100 °C, decreasing to 3.2 eV as the sample is heated to 150 °C, and subsequently rising to 3.5 eV with further heating to 300 °C.

Prior to heating, both the BMIMBF$_4$-modified perovskite films show a work function of 3.7 eV, lower than that measured for the pure perovskite and BMIMCl-modified perovskite films. For the BMIMBF$_4$-perovskite film, the work function decreases to 3.4 eV and 3.2 eV after heating the sample to 100 °C and 150 °C, respectively. Upon further increasing the temperature to 300 °C, the work function undergoes an upwards shift to 3.6 eV, similarly to the BMIMCl films. In contrast, the SnO$_2$/BMIMBF$_4$-perovskite film exhibits a consistent work function of 3.7 eV up to 100 °C. Beyond this point, the work function decreases to 3.4 at 150 °C and subsequently rises to 4.0 eV upon heating the sample to 300 °C.

Previous studies on the modification of ETLs with ILs have reported a reduction in the work function of ETLs.[13,49,50] This reduction is attributed to the introduction of dipoles on the ETL surface by the ILs. Noel et al.[49] reported a reduction in work function of both the SnO$_2$ ETL as well as the perovskite layer due to the doping of BMIMBF$_4$ in SnO$_2$. However, they associated the reduction in the perovskite work function to the shifting of the SnO$_2$ work function and could not identify any change in work function without the SnO$_2$ layer. Whilst the nature of the interaction between the SnO$_2$, IL and perovskite is difficult to determine conclusively from the XPS and work function data presented here, computational studies in the literature have calculated the strength of interaction between the BMIM$^+$ and BF_4^- ions with SnO$_2$ and perovskite, and this helps to explain our data.
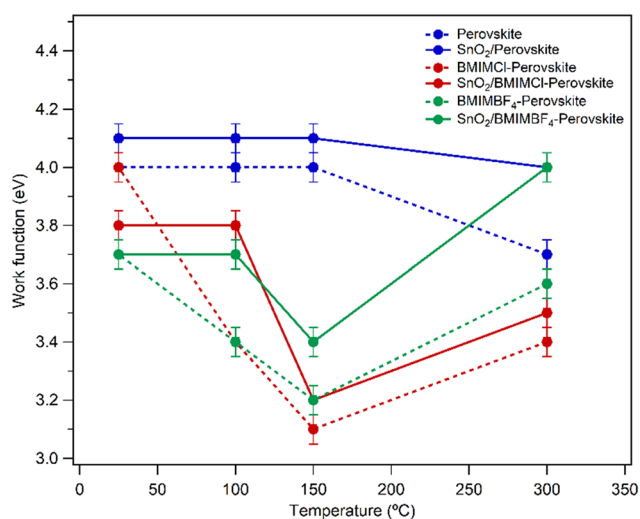

Fig. 5 Work function values of pure and IL-modified perovskite films as a function of temperature. Solid lines represent the films with a SnO$_2$ layer while the dashed lines represent films without the SnO$_2$ layer.

Liu et al.[51] used density functional theory (DFT) calculations to show that the BF_4^- anion has a stronger bond to SnO_2 whereas the $BMIM^+$ cation has a stronger bond to perovskite (using formamidinum lead iodide, $FAPbI_3$, as the perovskite in their calculations), which results in the formation of a dipole layer at the interface between the perovskite and SnO_2.

We attribute the lower work function values in the IL-modified films to the interaction between the ILs and the perovskite and/or the substrate. In the case of the $BMIMBF_4$-modified films, the BF_4^- anions can effectively bind to the substrate, passivating the substrate/perovskite interface, as demonstrated by Liu et al.[51] and Zhang et al.[19] (in the case of KBF_4). By doing so, these anions may remove some of the under-coordinated sites at the substrate/perovskite interface, which are known to be where photogenerated charge carriers are often trapped and lost to nonradiative recombination.[51] It is well-established that a positive surface dipole decreases the work function,[52] therefore, we suggest that the dipole caused by the interactions of the BF_4^- anions with the substrate and the $BMIM^+$ cations with the perovskite reduces the effective work function of the $BMIMBF_4$-modified samples.

The thermal energy from heating the films may facilitate the bonding between BF_4^- ions and the substrate, therefore decreasing the work function as the sample is heated to 150 °C. We propose that as the temperature increases to 300 °C, the BF_4^- ions are able to disassociate from the substrate, neutralising the dipole and leading to an increase in the work function of the $BMIMBF_4$-modified films. This may also be linked to the sudden appearance of Cl 2p peaks in the XPS spectra as the proposed $BMIMBF_4$ overlayer is disrupted at high temperature. The migration of BF_4^- ions away from the surface, rather than their loss from the film, is indicated by the observed shift of the B 1s peaks to lower BE after heating to 150 °C and 300 °C in the XPS measurements. DFT calculations have found that BF_4^- ions have a strong bond with SnO_2,[51] so it is likely that a much higher temperature is required for the BF_4^- ions to break free from the SnO_2 surface compared to the Ti foil substrate. This would explain why the Cl 2p peaks are only observed after the $SnO_2/BMIMBF_4$-perovskite film is heated to 300 °C, whereas they appear at 150 °C in the $BMIMBF_4$-perovskite film without SnO_2. This also coincides with the appearance of the low BE boron–carbide peaks at 300 °C in the C 1s spectra as the BF_4^- ions begin to interact with the perovskite film.

In the case of $BMIMCl$-modified films, the reduction in work function could be due to the chemical passivation of the perovskite film itself. This might result from the absence of dipole formation at the interface. It has previously been shown that Cl^- ions can diffuse into a perovskite lattice at a perovskite/SnO_2 interface, resulting in a better-matching of energy levels at the interface.[53] We hypothesise that $BMIM^+$ and Cl^- ions are able to diffuse into the perovskite grain boundaries, leading to an improvement in the crystallinity of the perovskite films. This may in turn reduce lattice stress and lower the work function.[54,55] The work functions of the

$BMIMCl$-modified films show a similar decreasing trend as the $BMIMBF_4$-modified films, decreasing up to 150 °C and then rising as the temperature is increased to 300 °C. We propose that the diffusion of $BMIMCl$ into the perovskite grain boundaries is facilitated as the temperature is increased to 150 °C, causing a decrease in the work function. It is not clear what causes the increase in the work function upon heating to 300 °C, but we tentatively suggest this could be due to thermal degradation. It must be noted that the magnitude of work function increase after heating the samples to 300 °C is smaller in the $BMIMCl$-modified films as compared to the $BMIMBF_4$-modified films. The constant values of work function up to 100 °C in all the films deposited on SnO_2 indicates the effectiveness of SnO_2 in preventing perovskite lattice stress, which can be induced by differences in thermal expansion coefficients of the perovskite and substrate.[54,55]

NEXAFS results

The carbon K-edge and nitrogen K-edge NEXAFS spectra recorded from a pure $BMIMBF_4$ film are shown in Fig. S3 in SI. These spectra were obtained during a previous beam run at the MAXLAB facility in Sweden (refer to (ref. 56) and details therein) and are used here for comparison with the IL-modified perovskite films. Limited literature is available on the NEXAFS of perovskites, and to our knowledge, none exists on IL-modified perovskite films. The C K-edge spectrum of the pure perovskite film is shown in Fig. 6a. The spectrum reveals two distinct signals at 285.0 eV and approximately 289.5 eV, denoted by Roman numerals I and III. Feature III is associated with C–N σ* bond transitions and has been documented in prior NEXAFS studies on perovskites.[57,58] The perovskite structure contains no unsaturated carbon bonds, so no π* peaks are anticipated in the NEXAFS spectra. Feature I at 285.0 eV is tentatively assigned to hydrocarbon contamination or X-ray beam damage. This feature has been a subject of debate and has been extensively discussed by Huang et al.[57] In their research, Huang et al. noted an increase in the intensity of the 285.0 eV signal upon repeated scanning of the same position on the perovskite sample, suggesting that beam damage could be causing this feature. However, they did not conclusively attribute this peak to beam damage as they also observed a weak peak at ~285 eV using bulk-sensitive fluorescence yield measurements and so they conclude the origin of the peak is uncertain. Other studies have attributed this feature to C–N σ* bond transitions (which usually appear at higher energies), while others have linked it to unspecified C=C π* transitions.[58,59] The C K-edge spectra of the IL-modified perovskite films reveal three distinct features, denoted as I, II, and III in Fig. 6a. Feature I, located at 285.0 eV, corresponds to adventitious carbon or beam damage. Feature III, observed at 289.5 eV, is attributed to C–N σ* transitions within the perovskite structure, as observed in the pure perovskite film. The second feature (II) identified

© 2025 The Author(s). Published by the Royal Society of Chemistry

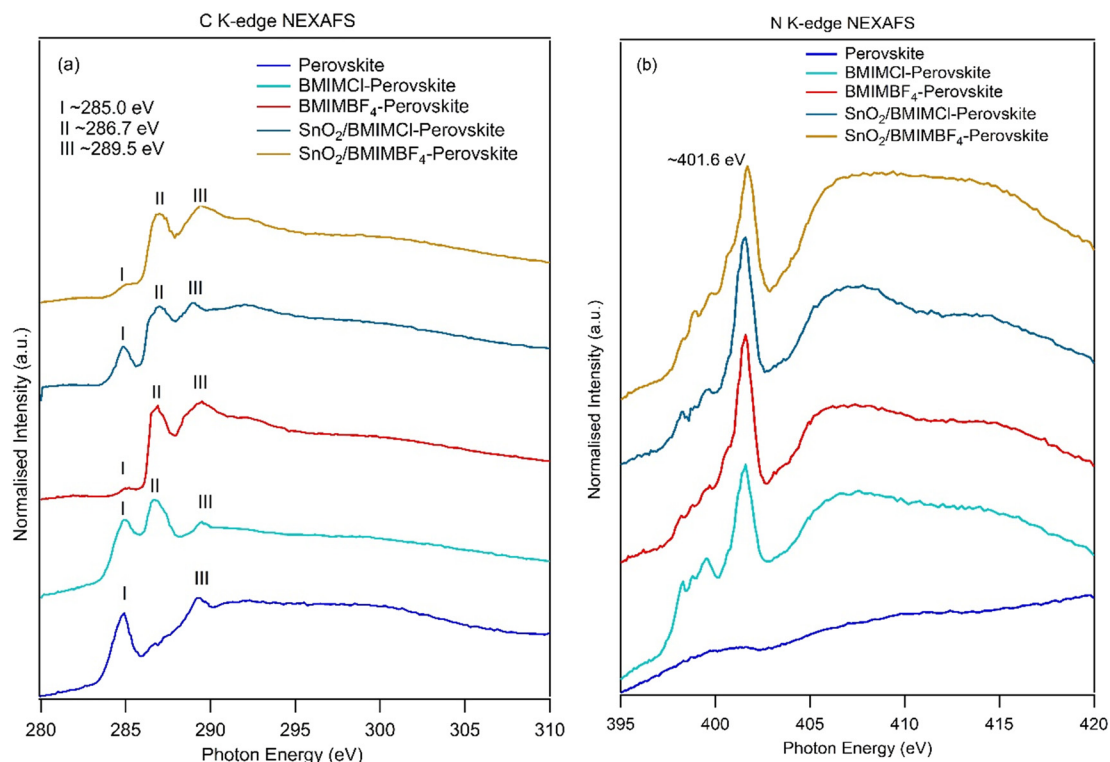RSC Appl. Interfaces, 2025, 2, 1674–1689 | 1681

Fig. 6 (a) C K-edge and (b) N K-edge NEXAFS spectra of pure and IL-modified perovskite films.

at 286.7 eV is associated with C 1s $\rightarrow \pi^*$ transitions, attributed to excitation from the carbon atoms within the imidazolium ring of the BMIM$^+$ cation. This observation aligns with the signal observed in the pure BMIMBF$_4$ NEXAFS spectrum (Fig. S3).

In the SnO$_2$/BMIMCl-perovskite film, both the perovskite peak (feature III) and the IL peak (feature II) have nearly identical intensities, with a minor feature at ~285.0 eV, which is associated with adventitious carbon/beam damage. Conversely, in the BMIMCl-perovskite film, the IL peak exhibits the highest intensity, accompanied by a relatively prominent adventitious carbon/beam damage peak, and a lower intensity perovskite peak relative to the SnO$_2$/BMIMCl-perovskite film. From the work function measurements in the previous section, the two BMIMCl-modified films started with different work function values prior to heating. We hypothesised from the work function measurements that BMIMCl is able to diffuse into the perovskite grain boundaries. The similar intensities of the perovskite and IL peaks in the C K edge spectra of the SnO$_2$/BMIMCl-perovskite film may imply a more balanced distribution of these components compared to the BMIMCl-perovskite film. This suggests that SnO$_2$ plays an important role in the interaction between the IL and the perovskite material. The two BMIMBF$_4$-modified films, which exhibited the same work function values before heating, also display very similar C K-edge spectra. In these spectra, feature I (~285.0 eV) is very small, indicating a higher resistance to beam damage or less adventitious carbon in these films. The perovskite peak

(feature III) is strong and is comparable in intensity to the IL signal (feature II).

Fig. 6b presents the N K-edge spectra of all the films. The N K edge spectrum from the pure perovskite film does not exhibit any π^* features, since the perovskite structure contains no unsaturated nitrogen bonds. A sharp

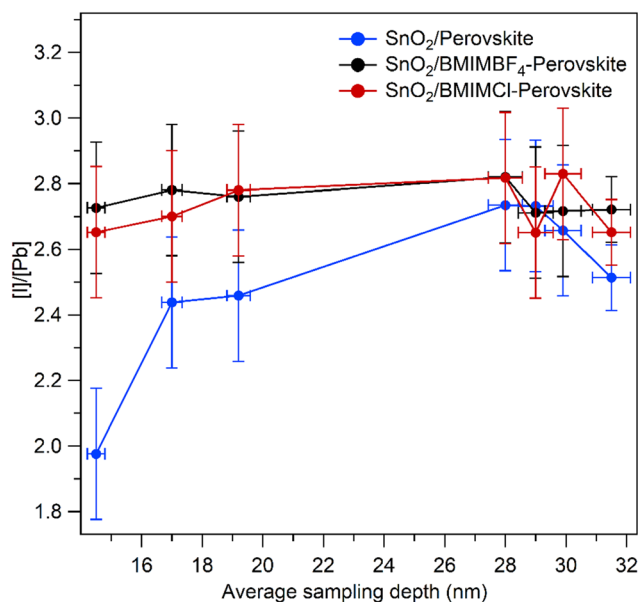**Fig. 7** I/Pb ratios from HAXPES as a function of averaging sampling depth for pure and IL-modified perovskite films on SnO$_2$.

1682 | *RSC Appl. Interfaces*, 2025, **2**, 1674–1689

© 2025 The Author(s). Published by the Royal Society of Chemistry

feature at ~401.6 eV is exhibited by all the IL-modified films and can be assigned to the N 1s → π* transitions corresponding to the two imidazolium ring nitrogen atoms as discussed for pure BMIMBF₄ in the SI. Broad σ* features can also be observed at higher photon energies. The N K-edge results confirm the presence of the IL in all the IL-modified films.

HAXPES results

The analysis so far suggests that IL-modified perovskite films on SnO₂-coated Ti substrates show significant stability. To explore their elemental distribution and bulk composition further, these films were analysed using HAXPES. The calculated I/Pb ratios, derived from both transmission and
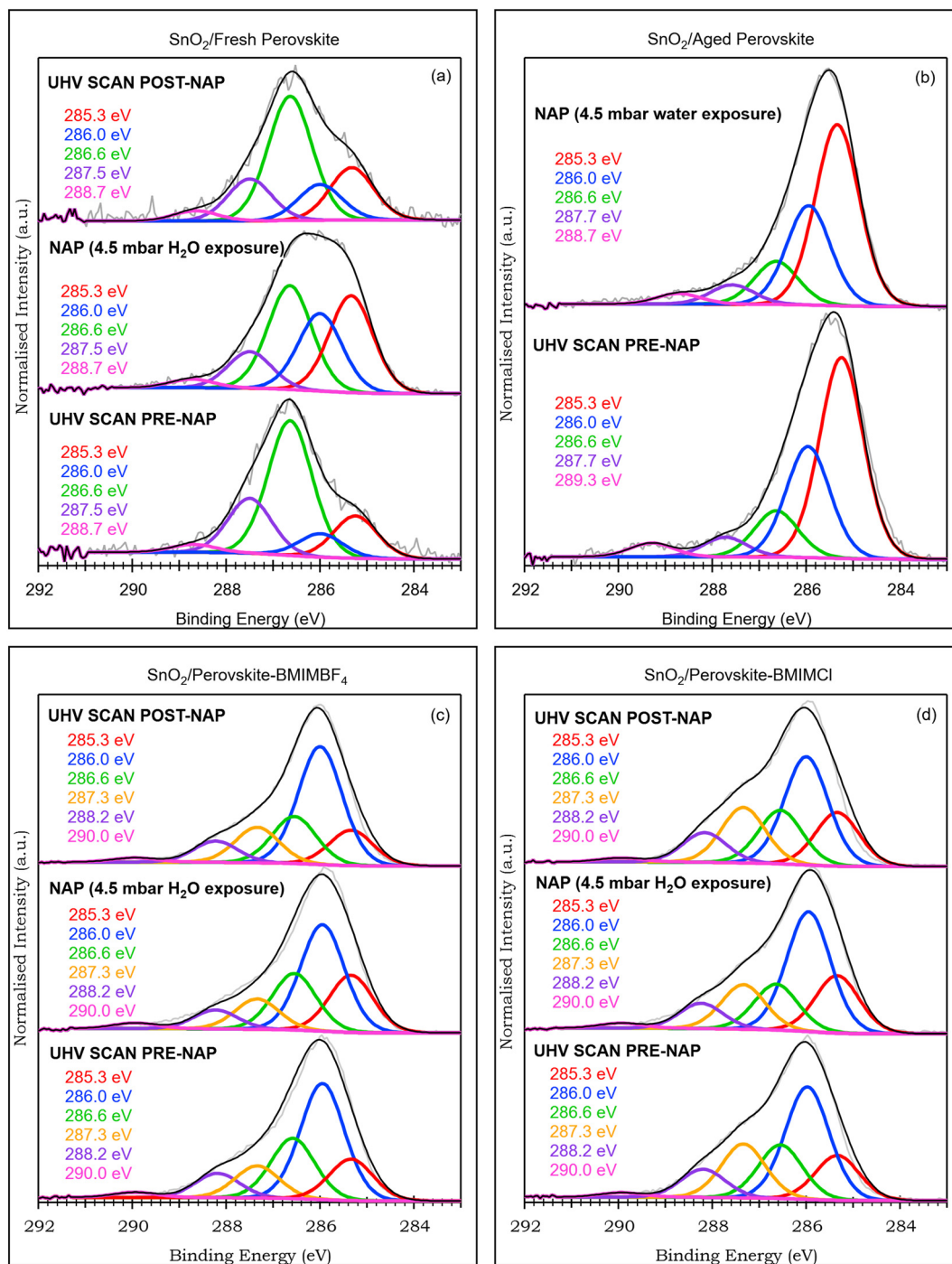
Fig. 8 High-resolution core level C 1s spectra of pure ((a) and (b)) and IL-modified ((c) and (d)) perovskite films on SnO₂ coated Ti foil measured before exposure, during exposure and after exposure to 4.5 mbar water vapour at room temperature. Spectral intensities are normalised to the intensity of the highest peak. BEs of fitted peaks are shown next to each spectrum and are assigned to the same chemical environments as described in Fig. 1.

© 2025 The Author(s). Published by the Royal Society of Chemistry

RSC Appl. Interfaces, 2025, **2**, 1674–1689 | **1683**

angular modes are plotted against average sampling depth in Fig. 7 (see sections 5 and 6 of SI for further explanation). It is important to note that the sampling depths for I 2p and Pb 3d levels differ due to their distinct photoelectron kinetic energies, so the average sampling depth is used in Fig. 7 (see sections 5 and 6 of SI for calculation of sampling depths). The spectra obtained from the transmission mode of the analyser (Fig. S5 in SI) correspond to the deepest sampling depth ($\sim$31.5 ± 0.6 nm) achievable with HAXPES. The contour plots of the I $2p_{3/2}$ and Pb $3d_{5/2}$ core level spectral intensities as a function of sampling depth, derived from the angular mode data are presented in Fig. S6 in SI. The I/Pb ratios plotted in Fig. 7 were calculated using slices from these contour plots (see Tables S3 and S4 in SI).

In the SnO$_2$/Perovskite film, the I/Pb ratio is 2.5 ± 0.1 at the maximum sampling depth of 31.5 ± 0.6 nm, consistent with the expected range of 2.5–2.9 for mixed halide perovskites. As the average sampling depth decreases to 29.9 ± 0.6 nm, the ratio slightly increases to 2.7 ± 0.2, remaining within the expected range. This value persists at decreasing probing depths of 29.0 ± 0.6 nm and 28.0 ± 0.6 nm. However, at the shallowest sampling depths of 19.2 ± 0.4 nm, 17.0 ± 0.3 nm, and 14.5 ± 0.3 nm, the I/Pb ratio progressively decreases to 2.5 ± 0.2, 2.4 ± 0.2, and 2.0 ± 0.2 respectively, with the latter suggesting degradation of the perovskite into PbI$_2$ at the surface. In the IL-modified perovskite films, the I/Pb ratios consistently range from 2.7 to 2.8 across all sampling depths, aligning with the nominal stoichiometry of mixed halide perovskites. This consistency indicates the structural integrity and stability throughout the IL-modified films and may suggest that both ILs help to passivate defects in the perovskite material and suppress its degradation.

NAP-XPS results

The moisture endurance of pure and IL-modified perovskite films deposited on SnO$_2$-coated Ti substrates was evaluated using NAP-XPS. Alongside films prepared a week prior, a fresh perovskite film was spin-coated onto a SnO$_2$-coated Ti substrate at the Henry Royce Facility and quickly transferred for NAP-XPS measurements. This fresh film, referred to as SnO$_2$/fresh-perovskite, allowed for the examination of the pure perovskite before surface degradation, while the week-old film is now termed SnO$_2$/aged-perovskite. Moisture-induced degradation was studied by exposing films to water vapour at 4.5 mbar, corresponding to 15% relative humidity at 25 °C. XPS spectra were recorded before, during, and after water exposure to assess moisture effects.

Fig. 8(a–d) presents the C 1s core level spectra for the four films. In the SnO$_2$/fresh-perovskite film (Fig. 8a), peaks at 285.3 eV, 286.0 eV, 286.6 eV, 287.5 eV, and 288.7 eV are observed, corresponding to adventitious carbon, MAI, the perovskite C–N bond, and hydrocarbon oxidation products (C═O and O–C═O), respectively. During water exposure, the intensity of the MAI and adventitious carbon peaks increases, suggesting the release of MA$^+$ ions. However, a reduction in

MAI peak intensity post-NAP hints at a potential reorganisation, possibly recovering the perovskite structure. Despite some fluctuation during water exposure, the perovskite peak remains dominant, highlighting the resilience of the material. Peaks at similar BE are observed in the SnO$_2$/aged-perovskite film (Fig. 8b), but here the adventitious carbon peak is the most intense, followed by the MAI peak, indicating significant surface degradation. The C–N perovskite peak shows reduced intensity compared to the fresh film, and no significant changes in peak intensities are seen during water exposure. The IL-modified perovskite films (Fig. 8c and d) show C 1s spectra with peaks at 285.3 eV, 286.0 eV, 286.6 eV, 287.3 eV, 288.2 eV and 290.0 eV corresponding to hydrocarbon contamination, aliphatic C–N bonds (from both MAI and/or the BMIM group), perovskite C–N and/or aromatic C–C–N bonds, imidazolic N–C–N carbon, C═O and O–C═O hydrocarbon oxidation products, respectively. Both IL-modified films exhibit similar spectra, with the 286.0 eV peak being the most intense. While the adventitious carbon peak increases during water exposure, the relative intensities of the perovskite and IL peaks remain largely unchanged, indicating minimal impact on the IL-modified perovskite films.

Fig. 9(a–d) illustrates the N 1s core level spectra for all films. In the SnO$_2$/fresh-perovskite film, a dominant peak at 402.6 eV and a weaker one at 400.5 eV are observed before, during, and after water exposure, corresponding to nitrogen in the perovskite and unreacted/dissociated MAI, respectively.[29,34] The perovskite peak intensity slightly decreases during water exposure but recovers post-exposure. The SnO$_2$/aged-perovskite film exhibits a low signal-to-noise ratio in its N 1s spectra, with weak peaks at 402.6 eV (perovskite) and 400.5 eV (MAI). Unlike the fresh film, these peaks are of nearly equal intensity, suggesting significant degradation before measurements. In the SnO$_2$/BMIMBF$_4$-perovskite film, peaks are fitted at 402.9 eV (perovskite), 401.6 eV (imidazole nitrogen in the IL), and 400.5 eV (MAI) before and after water exposure, with minor shifts during exposure.[30,31,60] The upward BE shift of the perovskite peak relative to pure films may be a result of IL-perovskite interactions. Furthermore, BE values for pure perovskite N 1s core levels have been reported in the literature in the range of 402.5–402.9 eV.[29,34,61–65] The SnO$_2$/BMIMCl-Perovskite film shows similar spectra with peaks at 402.8 eV (perovskite) and 401.6 eV (imidazole nitrogen in the IL) before and after water exposure, and a 400.5 eV peak (MAI) appearing in the NAP scan. The absence of MAI features in UHV scans suggests that BMIMCl may have either facilitated complete MAI conversion to perovskite during synthesis of the film or prevented its dissociation. The IL-modified perovskite films were deposited one week prior to the experiment, at the same time as the aged perovskite films. The N 1s spectra of the IL-modified films after one week of aging closely resemble that of the fresh perovskite film, indicating that the IL has effectively protected the perovskite from degradation.
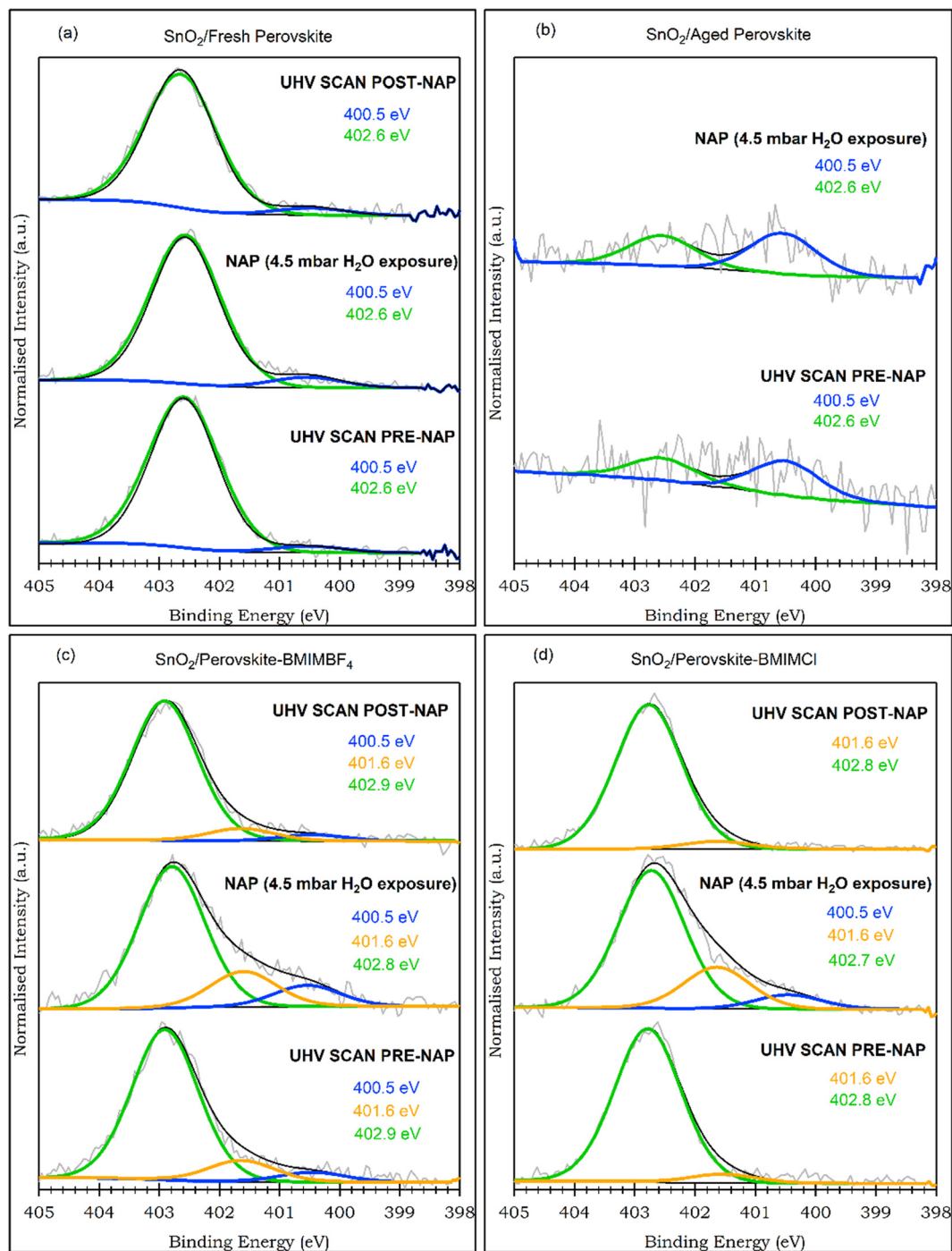
Fig. 9 High-resolution core level N 1s spectra of pure ((a) and (b)) and IL-modified ((c) and (d)) perovskite films on SnO_2 coated Ti foil measured before exposure, during exposure and after exposure to 4.5 mbar water vapour at room temperature. Spectral intensities are normalised to the intensity of the highest peak. Green coloured peaks at ~402.6 eV are assigned to nitrogen atoms in the perovskite structure, orange coloured peaks at ~401.6 eV are assigned to imidazole nitrogen atoms in the IL and blue coloured peaks at ~400.5 eV are assigned to nitrogen atoms in CH_3NH_3I (MAI).

The Pb 4f and I 3d core level spectra are presented and discussed in the SI (Fig. S7 and S8, respectively). In the Pb 4f spectra, the fresh perovskite film shows a +0.2 eV BE shift during water exposure, possibly indicating the formation of PbI_2 as a result of degradation.[66] The aged perovskite, however, appears to exhibit PbI_2 peaks from the outset, indicating that degradation had already occurred prior to the

measurements. During exposure of the aged perovskite to water, a weak doublet appears that is consistent with metallic lead.[66] This results from the decomposition of lead halides into metallic lead and halogen gas. The SnO_2/BMIMBF$_4$-perovskite film shows some shifts in BE on exposure to water but returns to its original BE after exposure. The SnO_2/BMIMCl-Perovskite film displays the most stable Pb 4f peaks,

with only a minor BE shift during water exposure. This suggests that the ILs may play a role in protecting or regenerating the perovskite structure, preventing further degradation. In the I 3d spectra, similar trends are observed. The fresh perovskite film undergoes a small positive BE shift, consistent with the Pb 4f results, and possibly pointing to the formation of PbI_2. The aged perovskite film, already degraded, shows only minor shifts in BE. The IL-modified films exhibit larger BE shifts during water exposure, followed by a return to near-original values after exposure.

The NAP-XPS results provide insightful perspectives into the moisture tolerance of IL-modified films. A comparative analysis of UHV scans before and after exposure to water vapor reveals the BMIMCl film exhibits the most promising behaviour in terms of moisture endurance. Notably, the Pb 4f and I 3d spectra of the BMIMCl film exhibit no upward BE shift, in contrast to the small positive BE shift observed in the Pb 4f spectra of the fresh perovskite film and the I 3d spectra of both the fresh perovskite and $BMIMBF_4$ films. During UHV scans, the absence of MAI peaks in the N 1s spectra of the BMIMCl film before and after water exposure, indicates complete regeneration of the perovskite upon removal from the water environment. This observation aligns well with the I 3d and Pb 4f spectra, where BE values return to pre-NAP levels after water exposure. In contrast, both the fresh perovskite and $BMIMBF_4$ films exhibit a weak MAI feature in both UHV and NAP scans.

The shifts in Pb 4f, N 1s, and I 3d peaks, initially to lower BE during NAP and then to higher BE in the UHV scan post-NAP, are very small but may be important (the fitted components have an error of ±0.1 eV in BE, so the shifts are at the limit of what is statistically significant). This phenomenon is more pronounced in the $BMIMBF_4$ film compared to the BMIMCl film. These observations may be explained using our initial hypothesis that the incorporation of $BMIMBF_4$ into the perovskite results in the formation of an overlayer on the perovskite surface. The strong interaction between $BMIM^+$ cations and I^- ions of the perovskite may increase the miscibility of the BMIM group in water, supported by previous findings indicating that halide ions enhance the miscibility of $BMIMBF_4$ in water.[67] This may lead to water intercalation with surface $BMIM^+$ cations. A hydrogen bonding interaction between H^+ ions of water and iodide ions of the perovskite may increase the BE of the I 3d electrons and weaken the Pb–I bond causing a decrease in BE of Pb 4f electrons. Weakening of Pb–I bonds may result in a lowering of N 1s BE of MA^+ cations and facilitate the loss of MA^+ cations from the perovskite lattice, which would explain the observed increase in the intensity of the MAI peak in NAP spectra. After water exposure, $BMIM^+$ cations may rearrange, leading to the reformation of the overlayer and the reverse BE changes. In the case of the BMIMCl film, the more homogeneous distribution of $BMIM^+$ cations across the depth of the film may not favour the intercalation of water molecules. In imidazolium-based ILs, the anion has been found to have a greater influence than the cation on the

hydrophobicity/hydrophilicity of the IL.[68] The hydrophobicity of the anion affects the network formation of the water and hence the miscibility of the IL.[69] When water is added to ILs, the cation–anion networks are broken and new water–cation/anion networks are formed. Chang *et al.* used molecular dynamics simulations to show that the addition of water to $BMIMBF_4$ alters its structural organisation by disrupting the cation–anion network.[70] Feng *et al.* used molecular dynamics to show that changing the anion from BF_4^- to Cl^- alters the water distribution in the IL and slows the diffusion of cations and water molecules.[71] They attribute this to the stronger electrostatic interaction of the Cl^- anion with the other particles in the IL/water mixture. Therefore, the Cl^- anion is likely to play a role in protecting the BMIMCl-perovskite film from water ingress. BMIMCl appears to be more effective in protecting the perovskite from moisture ingress but leaves it more prone to thermal degradation as observed in the XPS analysis. The choice of anion in the IL is clearly an important factor in determining the stability of the perovskite film. It is worth mentioning, however, that an improvement in the stability of the perovskite film does not necessarily lead to an improvement in the efficiency of the device. Therefore, it is important that the performance of IL-modified solar cells are characterised alongside fundamental studies of stability.

The XPS results indicate that the mixed halide perovskite ink utilised in this study exhibits some resistance to thermal degradation up to a temperature of 150 °C. This is evident from the presence of perovskite phase peaks observed in the spectra recorded before and after heating to temperatures of 100 °C and 150 °C across all the studied films. The XPS analysis further reveals the presence of the perovskite phase in the IL-modified films deposited on SnO_2-coated Ti substrates even at 300 °C. This underscores the significant role played by both the SnO_2 ETL layer and the ILs, BMIMCl and $BMIMBF_4$, in conferring stability to the perovskite even at elevated temperatures of 300 °C. The results from the work function measurements aid in comprehending how the two ILs interact with the perovskite and the degradation of the pure perovskite films upon heating to 300 °C. We hypothesise that $BMIMBF_4$ forms a protective overlayer on the perovskite surface, a process facilitated by the stronger interaction of the BF_4^- ions with the SnO_2 layer. This hypothesis explains the superior thermal stability of the $SnO_2/BMIMBF_4$-perovskite film. It is possible that this IL overlayer might act as an interfacial modifier when incorporated into a device structure, which might help to improve energy level matching and passivate defects at interfaces. In contrast, BMIMCl is able to diffuse into the perovskite grain boundaries, neutralising some of the surface defect sites and enhancing the crystallinity of the film. Constant work function values observed up to 150 °C in all the films with an underlying SnO_2 layer indicate that SnO_2 is important in mitigating lattice stress induced by differences in the thermal expansion coefficients of the perovskite and the Ti substrate.

The NEXAFS results confirm the presence of the perovskite phase in the pure perovskite film before heat

treatment. NEXAFS spectra show individual and distinct features corresponding to the IL and perovskite. The relative intensity of these features indicate that the SnO_2 layer may be significant in facilitating the incorporation of BMIMCl into the perovskite. NEXAFS results confirm the stability of both $BMIMBF_4$-modified perovskite films, aligning with observations from XPS and work function analyses. The HAXPES findings illustrate that the observed degradation in the pure perovskite film is predominantly a surface phenomenon, with the I/Pb ratio decreasing from the nominal perovskite stoichiometry to the lead halide ratio as the probing depth decreases. Consistent I/Pb ratios obtained from HAXPES measurements for the IL-modified films across different probing depths further affirm the superior stability of the IL-modified films across the depth of the film. The NAP-XPS findings indicate that the IL-modified films demonstrate favourable stability when exposed to water. Specifically, the BMIMCl-modified films may show greater resistance to moisture penetration compared to the $BMIMBF_4$-modified films.

Heat and moisture are key environmental stressors contributing to the instability of perovskite solar cells. Our results indicate that IL-modified perovskites have increased stability to both. These results are particularly valuable because there is an extensive body of literature discussing the performance of IL-modified perovskites, however, there are very few fundamental studies that focus on their structural stability. Our study bridges this gap by providing a deeper understanding of how these modifications affect the structural integrity of perovskite films.

4. Conclusions

A combination of surface science techniques has been employed to investigate the stability of ionic liquid-modified mixed-halide perovskite films against heat and moisture. XPS results demonstrate that the $MAPbI_{3-x}Cl_x$ is stable up to 150 °C, with perovskite phase peaks present before and after heating. IL-modified films on SnO_2 show even greater thermal stability, maintaining the perovskite phase at 300 °C. Work function measurements reveal that both SnO_2 and the ILs (BMIMCl and $BMIMBF_4$) play key roles in this stability. $BMIMBF_4$ appears to form a protective layer over the perovskite surface, while BMIMCl integrates into the grain boundaries, enhancing crystallinity. For the IL-modified films, HAXPES results show consistent I/Pb ratios across different depths, whereas the pure perovskite exhibits degradation at the surface level. NAP-XPS results illustrate that the IL-modified films exhibit improved moisture resistance, with BMIMCl-modified films showing greater protection. This study bridges a crucial gap by focusing on the structural stability of IL-modified perovskites, offering valuable insights into how these modifications enhance both thermal and moisture resistance and advancing their potential for commercial application.

Author contributions

The manuscript was written through contributions of all authors. All authors have given approval to the final version of the manuscript.

Conflicts of interest

There are no conflicts to declare.

Data availability

Supplementary information is available: Fig. S1: A schematic representation of the six samples used in this study. The top three show the perovskite and IL-modified perovskite films deposited on SnO_2-coated Ti foil substrate, while the bottom three show the samples deposited directly onto Ti substrate without a layer of SnO_2; Table S1: Photon energies used in acquiring the XPS spectra on the AU-MATline beamline; Table S2: Binding energies of the I $4d_{5/2}$ component for each sample, used to plot the I 4d spectra in Fig. 3 of the main text; Figure S2: SECO spectra and corresponding work function values of samples before and after heating. Solid lines represent the samples with a SnO_2 layer while the dashed lines represent samples without the SnO_2 layer; Fig. S3: C K-edge (a) and N K-edge (b) NEXAFS spectra of $BMIMBF_4$; Fig. S4: Sample configuration for measuring photoelectrons from different photoelectron emission angles (θ); Table S3: Analyser angular ranges from which the HAXPES data was binned and corresponding photoelectron emission angles (from the surface normal); Fig. S5 High-resolution (a) I $2p_{3/2}$ and (b) Pb $3d_{5/2}$ core-level spectra of the pure and IL-modified perovskite samples measured using the transmission mode of HAXPES. Here the peaks are intensity normalised with respect to Pb $3d_{5/2}$; Fig. S6 Contour plots showing I $2p_{3/2}$ and Pb $3d_{5/2}$ core level intensities from angular mode measurements. The contour plots show the ±25° angular range from the analyser on the y axis (an arrow indicating increasing sampling depth is shown) and binding energy on the x axis; Table S4: I/Pb ratios of the films as a function of the HAXPES probing depth; Fig. S7 High-resolution core level Pb 4f spectra of pure and IL-modified perovskite samples measured before exposure, during exposure and after exposure to 4.5 mbar water vapour at room temperature; Fig. S8 High-resolution core level I 3d spectra of pure and IL-modified perovskite samples measured before exposure, during exposure and after exposure to 4.5 mbar water vapour at room temperature. See DOI: **https://doi.org/10.1039/D5LF00206K**.

The data that support the findings of this study are openly available at the following URL/DOI: **https://uclandata.uclan.ac.uk/id/eprint/536**.

Acknowledgements

© 2025 The Author(s). Published by the Royal Society of Chemistry

RSC Appl. Interfaces, 2025, **2**, 1674–1689 | 1687

References

1 C. Liu, Y. Yang, H. Chen, J. Xu, A. Liu, A. S. R. Bati, H. Zhu, L. Grater, S. S. Hadke, C. Huang, V. K. Sangwan, T. Cai, D. Shin, L. X. Chen, M. C. Hersam, C. A. Mirkin, B. Chen, M. G. Kanatzidis and E. H. Sargent, *Science*, 2023, **382**, 810–815.

2 D. Liu, W. Zhang, Z. Ren and X. Li, *RSC Adv.*, 2022, **12**, 14631–14638.

3 Y. Bai, Q. Dong, Y. Shao, Y. Deng, Q. Wang, L. Shen, D. Wang, W. Wei and J. Huang, *Nat. Commun.*, 2016, **7**, 12806.

4 G. Grancini, C. Roldán-Carmona, I. Zimmermann, E. Mosconi, X. Lee, D. Martineau, S. Narbey, F. Oswald, F. De Angelis, M. Graetzel and M. K. Nazeeruddin, *Nat. Commun.*, 2017, **8**, 15684.

5 C.-T. Lin, S. Pont, J. Kim, T. Du, S. Xu, X. Li, D. Bryant, M. A. McLachlan and J. R. Durrant, *Sustainable Energy Fuels*, 2018, **2**, 1686–1692.

6 G. Yang, Z. Ren, K. Liu, M. Qin, W. Deng, H. Zhang, H. Wang, J. Liang, F. Ye, Q. Liang, H. Yin, Y. Chen, Y. Zhuang, S. Li, B. Gao, J. Wang, T. Shi, X. Wang, X. Lu, H. Wu, J. Hou, D. Lei, S. K. So, Y. Yang, G. Fang and G. Li, *Nat. Photonics*, 2021, **15**, 681–689.

7 X. Liu, J. Min, Q. Chen, T. Liu, G. Qu, P. Xie, H. Xiao, J.-J. Liou, T. Park and Z.-X. Xu, *Angew. Chem., Int. Ed.*, 2022, **61**, e202117303.

8 F. Wang, D. Duan, M. Singh, C. M. Sutter-Fella, H. Lin, L. Li, P. Naumov and H. Hu, *Energy Environ. Mater.*, 2022, e12435.

9 M. Shahiduzzaman, E. Y. Muslih, A. K. M. Hasan, L. Wang, S. Fukaya, M. Nakano, M. Karakawa, K. Takahashi, M. Akhtaruzzaman, J.-M. Nunzi and T. Taima, *Chem. Eng. J.*, 2021, **411**, 128461.

10 S. Colella, E. Mosconi, P. Fedeli, A. Listorti, F. Gazza, F. Orlandi, P. Ferro, T. Besagni, A. Rizzo, G. Calestani, G. Gigli, F. De Angelis and R. Mosca, *Chem. Mater.*, 2013, **25**, 4613–4618.

11 H. Yu, F. Wang, F. Xie, W. Li, J. Chen and N. Zhao, *Adv. Funct. Mater.*, 2014, **24**, 7102–7108.

12 Q. Yang, Z. Zhang, X.-G. Sun, Y.-S. Hu, H. Xing and S. Dai, *Chem. Soc. Rev.*, 2018, **47**, 2020–2064.

13 D. Yang, X. Zhou, R. Yang, Z. Yang, W. Yu, X. Wang, C. Li, S. Liu and R. P. H. Chang, *Energy Environ. Sci.*, 2016, **9**, 3071–3078.

14 Y. Zhang, Z. Fei, P. Gao, Y. Lee, F. F. Tirani, R. Scopelliti, Y. Feng, P. J. Dyson and M. K. Nazeeruddin, *Adv. Mater.*, 2017, **29**, 1702157.

15 S. Bai, P. Da, C. Li, Z. Wang, Z. Yuan, F. Fu, M. Kawecki, X. Liu, N. Sakai, J. T.-W. Wang, S. Huettner, S. Buecheler, M. Fahlman, F. Gao and H. J. Snaith, *Nature*, 2019, **571**, 245–250.

16 P.-C. Huang, T.-J. Yang, C.-J. Lin, M.-Y. Wang and W.-C. Lin, *Langmuir*, 2024, **40**, 11873–11887.

17 L. Fan, Y. Ding, J. Luo, B. Shi, X. Yao, C. Wei, D. Zhang, G. Wang, Y. Sheng, Y. Chen, A. Hagfeldt, Y. Zhao and X. Zhang, *J. Mater. Chem. A*, 2017, **5**, 7423–7432.

18 L. Yang, D. Wu, J. Tang, Y. Hao, J. Wang, X. Zhao and P. Yang, *Chem. Phys. Lett.*, 2020, **754**, 137638.

19 J. Zhang, S. Wu, T. Liu, Z. Zhu and A. K. Y. Jen, *Adv. Funct. Mater.*, 2019, **29**, 1808833.

20 Q. Chen, H. Zhou, Y. Fang, A. Z. Stieg, T.-B. Song, H.-H. Wang, X. Xu, Y. Liu, S. Lu, J. You, P. Sun, J. McKay, M. S. Goorsky and Y. Yang, *Nat. Commun.*, 2015, **6**, 7269.

21 Z. Lian, Q. Yan, T. Gao, J. Ding, Q. Lv, C. Ning, Q. Li and J.-l. Sun, *J. Am. Chem. Soc.*, 2016, **138**, 9409–9412.

22 H. Zhang, Q. Liao, X. Wang, K. Hu, J. Yao and H. Fu, *Small*, 2016, **12**, 3780–3787.

23 H. Min, M. Kim, S.-U. Lee, H. Kim, G. Kim, K. Choi, J. H. Lee and S. I. Seok, *Science*, 2019, **366**, 749–753.

24 J. W. Kim and A. Kim, *Curr. Appl. Phys.*, 2021, **31**, 52–59.

25 A. Regoutz, M. Mascheck, T. Wiell, S. K. Eriksson, C. Liljenberg, K. Tetzner, B. A. D. Williamson, D. O. Scanlon and P. Palmgren, *Rev. Sci. Instrum.*, 2018, **89**, 073105.

26 B. F. Spencer, S. Maniyarasu, B. P. Reed, D. J. H. Cant, R. Ahumada-Lazo, A. G. Thomas, C. A. Muryn, M. Mascheck, S. K. Eriksson, T. Wiell, T. L. Lee, S. Tougaard, A. G. Shard and W. R. Flavell, *Appl. Surf. Sci.*, 2021, **541**, 148635.

27 D. J. H. Cant, B. F. Spencer, W. R. Flavell and A. G. Shard, *Surf. Interface Anal.*, 2022, **54**, 442–454.

28 F. Okejiri, J. Fan, Z. Huang, K. M. Siniard, M. Chi, F. Polo-Garzon, Z. Yang and S. Dai, *iScience*, 2022, **25**, 104214.

29 B. Philippe, B.-W. Park, R. Lindblad, J. Oscarsson, S. Ahmadi, E. M. J. Johansson and H. Rensmo, *Chem. Mater.*, 2015, **27**, 1720–1731.

30 V. Lockett, R. Sedev, C. Bassell and J. Ralston, *Phys. Chem. Chem. Phys.*, 2008, **10**, 1330–1335.

31 S. Caporali, U. Bardi and A. Lavacchi, *J. Electron Spectrosc. Relat. Phenom.*, 2006, **151**, 4–8.

32 B.-w. Park, H. W. Kwon, Y. Lee, D. Y. Lee, M. G. Kim, G. Kim, K.-j. Kim, Y. K. Kim, J. Im, T. J. Shin and S. I. Seok, *Nat. Energy*, 2021, **6**, 419–428.

33 A. Calloni, A. Abate, G. Bussetti, G. Berti, R. Yivlialin, F. Ciccacci and L. Duò, *J. Phys. Chem. C*, 2015, **119**, 21329–21335.

34 K. X. Steirer, P. Schulz, G. Teeter, V. Stevanovic, M. Yang, K. Zhu and J. J. Berry, *ACS Energy Lett.*, 2016, **1**, 360–366.

35 Z. Ahmad, M. Najeeb Nellikkal, R. Shakoor, A. Ashraf, S. Al-Muhtaseb, A. Soliman and M. Nazeeruddin, *Sci. Rep.*, 2017, **7**, 15406.

36 J.-W. Lee, Z. Dai, T.-H. Han, C. Choi, S.-Y. Chang, S.-J. Lee, N. De Marco, H. Zhao, P. Sun, Y. Huang and Y. Yang, *Nat. Commun.*, 2018, **9**, 3021.

37 T. Cao, P. Huang, Z. Kaicheng, Z. Sun, K. Zhu, L. Yuan, K. Chen, N. Chen and Y. Li, *J. Mater. Chem. A*, 2018, **6**, 3435–3443.

38 P. Chen, Y. Bai, S. Wang, M. Lyu, J.-H. Yun and L. Wang, *Adv. Funct. Mater.*, 2018, **28**, 1706923.

39 C. Rocks, V. Svrcek, P. Maguire and D. Mariotti, *J. Mater. Chem. C*, 2017, **5**, 902–916.

40 B. Matsoso, K. Ranganathan, B. Mutuma, T. Lerotholi, G. Jones and N. Coville, *New J. Chem.*, 2017, **41**, 9497–9504.

41 M. Kot, C. Das, K. Henkel, K. Wojciechowski, H. Snaith and D. Schmeißer, *Nucl. Instrum. Methods Phys. Res., Sect. B*, 2017, **411**, 49–52.

42 W.-C. Lin, W.-C. Lo, J.-X. Li, Y.-K. Wang, J.-F. Tang and Z.-Y. Fong, *npj Mater. Degrad.*, 2021, **5**, 13.

43 X. Yan, W. Fan, F. Cheng, H. Sun, C. Xu, L. Wang, Z. Kang and Y. Zhang, *Nano Today*, 2022, **44**, 101503.

44 D. W. deQuilettes, W. Zhang, V. M. Burlakov, D. J. Graham, T. Leijtens, A. Osherov, V. Bulović, H. J. Snaith, D. S. Ginger and S. D. Stranks, *Nat. Commun.*, 2016, **7**, 11683.

45 J. H. Heo, M. H. Lee, M. H. Jang and S. H. Im, *J. Mater. Chem. A*, 2016, **4**, 17636–17642.

46 Y. Liu, Y. Zhao, S. Xu and S. Cao, *Polymer*, 2015, **77**, 42–47.

47 I. J. Villar-Garcia, E. F. Smith, A. W. Taylor, F. Qiu, K. R. J. Lovelock, R. G. Jones and P. Licence, *Phys. Chem. Chem. Phys.*, 2011, **13**, 2797–2808.

48 M. Caputo, N. Cefarin, A. Radivo, N. Demitri, L. Gigli, J. R. Plaisier, M. Panighel, G. Di Santo, S. Moretti, A. Giglia, M. Polentarutti, F. De Angelis, E. Mosconi, P. Umari, M. Tormen and A. Goldoni, *Sci. Rep.*, 2019, **9**, 15159.

49 N. K. Noel, S. N. Habisreutinger, B. Wenger, Y.-H. Lin, F. Zhang, J. B. Patel, A. Kahn, M. B. Johnston and H. J. Snaith, *Adv. Energy Mater.*, 2020, **10**, 1903231.

50 K. Zhang, X. Zhang, K. G. Brooks, B. Ding, S. Kinge, Y. Ding, S. Dai and M. K. Nazeeruddin, *Sol. RRL*, 2023, **7**, 2300115.

51 D. Liu, H. Zheng, Y. Ahmed, C. Zheng, Y. Wang, H. Chen, L. Chen and S. Li, *J. Power Sources*, 2022, **519**, 230814.

52 R. Jacobs, J. Booske and D. Morgan, *Adv. Funct. Mater.*, 2016, **26**, 5471–5482.

53 H. Jiang, J. Zhang, C. Peng, K. Dong, Z. Wei, W. Jiang, Z. Long and Z. Zhou, *Small*, 2025, **21**, 2500240.

54 Y. Wang, D. Zheng, K. Wang, Q. Yang, J. Qian, J. Zhou, S. Liu and D. Yang, *Angew. Chem., Int. Ed.*, 2024, **63**, e202405878.

55 W. He, X. Yang, J. Duan, J. Zhang, Q. Guo, H. Huang and Q. Tang, *J. Colloid Interface Sci.*, 2023, **646**, 695–702.

56 M. Wagstaffe, M. J. Jackman, K. L. Syres, A. Generalov and A. G. Thomas, *ChemPhysChem*, 2016, **17**, 3430–3434.

57 W. Huang, F. Huang, E. Gann, Y.-B. Cheng and C. R. McNeill, *Adv. Funct. Mater.*, 2015, **25**, 5529–5536.

58 M.-C. Jung, Y. M. Lee, H.-K. Lee, J. Park, S. R. Raga, L. K. Ono, S. Wang, M. R. Leyden, B. D. Yu, S. Hong and Y. Qi, *Appl. Phys. Lett.*, 2016, **108**, 073901.

59 J. A. McLeod, Z. Wu, P. Shen, B. Sun and L. Liu, *J. Phys. Chem. Lett.*, 2014, **5**, 2863–2867.

60 O. Olivares-Xometl, N. V. Likhanova, M. A. Domínguez-Aguilar, J. M. Hallen, L. S. Zamudio and E. Arce, *Appl. Surf. Sci.*, 2006, **252**, 2139–2152.

61 R. D. Raninga, R. A. Jagt, S. Béchu, T. N. Huq, W. Li, M. Nikolka, Y.-H. Lin, M. Sun, Z. Li, W. Li, M. Bouttemy, M. Frégnaux, H. J. Snaith, P. Schulz, J. L. MacManus-Driscoll and R. L. Z. Hoye, *Nano Energy*, 2020, **75**, 104946.

62 Y. Li, X. Xu, C. Wang, C. Wang, F. Xie, J. Yang and Y. Gao, *J. Phys. Chem. C*, 2015, **119**, 23996–24002.

63 J. Chun-Ren Ke, A. S. Walton, D. J. Lewis, A. Tedstone, P. O'Brien, A. G. Thomas and W. R. Flavell, *Chem. Commun.*, 2017, **53**, 5231–5234.

64 L. Liu, J. A. McLeod, R. Wang, P. Shen and S. Duhm, *Appl. Phys. Lett.*, 2015, **107**, 061904.

65 F. Arabpour Roghabadi, V. Ahmadi and K. Oniy Aghmiuni, *J. Phys. Chem. C*, 2017, **121**, 13532–13538.

66 S. Maniyarasu, J. C.-R. Ke, B. F. Spencer, A. S. Walton, A. G. Thomas and W. R. Flavell, *ACS Appl. Mater. Interfaces*, 2021, **13**, 43573–43586.

67 H.-M. Lin, H.-Y. Tien, Y.-T. Hone and M.-J. Lee, *Fluid Phase Equilib.*, 2007, **253**, 130–136.

68 M. G. Freire, L. M. N. B. F. Santos, A. M. Fernandes, J. A. P. Coutinho and I. M. Marrucho, *Fluid Phase Equilib.*, 2007, **261**, 449–454.

69 T. Méndez-Morales, J. Carrete, Ó. Cabeza, L. J. Gallego and L. M. Varela, *J. Phys. Chem. B*, 2011, **115**, 6995–7008.

70 T.-M. Chang and S. E. Billeck, *J. Phys. Chem. B*, 2021, **125**, 1227–1240.

71 S. Feng and G. A. Voth, *Fluid Phase Equilib.*, 2010, **294**, 148–156.

© 2025 The Author(s). Published by the Royal Society of Chemistry

RSC Appl. Interfaces, 2025, **2**, 1674–1689 | **1689**